Calculation of vertical and horizontal mobilities in InAs/GaSb superlattices

F. Szmulowicz,[1,*] H. J. Haugan,[2] S. Elhamri,[3] and G. J. Brown[4]
[1]*University of Dayton Research Institute, 300 College Park Avenue, Dayton, Ohio 45469-0178, USA*
[2]*Universal Technologies Corporation, Dayton, Ohio 45432-2600, USA*
[3]*Department of Physics, University of Dayton, Dayton, Ohio 45469-2314, USA*
[4]*Materials and Manufacturing Directorate, Air Force Research Laboratory, WPAFB, Ohio 45433-7707, USA*
(Received 16 August 2011; published 13 October 2011)

Superlattice (SL) devices such as infrared detectors and quantum-cascade lasers rely on efficient transport of carriers perpendicular to the SL layers by drift and/or diffusion. While horizontal mobilities are measured routinely, measurements of perpendicular-carrier mobilities require nonstandard experimental techniques such as the geometric magneto-resistance. Here we show how perpendicular mobilities can be estimated from horizontal mobility measurements and calculated mobilities. We treat low-temperature horizontal and vertical transport in SL on an equal footing by calculating both mobilities using the same interface roughness scattering (IRS) model from a rigorous solution of the Boltzmann transport equation. The calculation is specialized to the case of InAs/GaSb SLs, which are of current interest in the development of third-generation infrared detector focal plane arrays. The results are compared to available data.

DOI: 10.1103/PhysRevB.84.155307 PACS number(s): 73.90.+f, 73.50.Dn, 73.21.Cd

I. INTRODUCTION

The relationship between vertical and horizontal transport in superlattices (SLs) has received renewed interest because of type-II InAs/GaSb SLs, which are promising materials for third-generation infrared focal-plane arrays and photodiodes.[1–10] The performance of such devices requires high vertical carrier mobilities for efficient carrier transport through drift and/or diffusion. However, vertical mobilities are not measured routinely since their measurement requires nonstandard and indirect experimental techniques such as the geometric magneto-resistance.[11,12] Indeed, what is known about vertical mobility is often inferred indirectly from fitting current-voltage data.[13] Here we develop the necessary formalism for the calculation of low-temperature vertical and horizontal mobilities and specialize it to the case of InAs/GaSb SLs. Then we show how the model results and measured in-plane mobilities can be used to infer the values of vertical mobilities for later use in device modeling and materials improvement.

In InAs/GaSb SLs, hole transport in the growth direction is inefficient since the valence bands are relatively flat and the corresponding hole mass very large.[14] On the other hand the electron mass is small, on the order of the bulk mass in InAs ($m = 0.024m_0$), and electron motion is diffusive, being limited by the usual scattering mechanisms such as interface roughness scattering (IRS),[15] phonon scattering,[16] and point- or extended-defect scattering.[17] Hence, SL devices rely mainly on electron transport for charge movement. Since vertical and horizontal electron transport in SLs is limited by the same scattering mechanisms, one should calculate them using the same transport model so as to compare them quantitatively and qualitatively.

While there has been a great deal of work on in-plane transport in quantum wells,[18] there has been no comparable effort in SL transport, especially addressing both vertical and horizontal mobilities and applying the results to a realistic system of current interest.[19] The theory of diffusive carrier transport in SLs was developed by Mori and Ando,[20] Dharssi and Butcher,[21] and others.[22,23] Most theoretical and experimental developments to date concern horizontal transport.[24] Here we address ourselves to the issue of both the vertical and horizontal transport in SLs, develop the required formalism, explore its properties, and apply it to the calculation of vertical and horizontal mobilities in InAs/GaSb SLs.

This paper is organized as follows. In Sec. II the relevant formalism for both the vertical and horizontal mobilities in SLs is derived. Since the relevant literature is scattered over many publications or is incomplete, this paper will try to be self-contained by providing the salient detail in one place. In the case of IRS limited mobility it will be shown that in absence of screening, the in-plane relaxation rates are smaller than the vertical relaxation rates; hence, in general, if the carrier masses were isotropic, horizontal mobilities would be larger than vertical mobilities. Then, in Sec. III in-plane and vertical-electron mobilities are calculated for a range of SL and roughness parameters relevant to transport in InAs/GaSb SLs.

II. ANALYTICAL DEVELOPMENT

Because of the large hole masses of the bulk constituents of the InAs/GaSb SL, the topmost heavy hole band in the SL is nearly dispersionless in the growth direction, resulting in the hole effective mass several orders of magnitude larger than the electron mass.[14] As a result, holes are immobile and largely confined to the GaSb layer, contributing negligibly to the vertical current in SL devices such as p-n or p-i-n photodetectors. Since the photocurrent in such devices is carried mainly by electrons, the present treatment is specialized to electrons.

A transport calculation comprises several components, each of which is treated in turn subsequently: the calculation of the energy bands and wave functions—Sec. A; the identification and the mathematical treatment of the relevant scattering mechanisms (here IRS)—Sec. B; the calculation of the scattering rates—Sec. C; the solution of the Boltzmann equation—Sec. D; development of expressions for IRS relaxation

rates—Sec. E; development of expressions for the mobilities and proof of a theorem relating vertical and horizontal relaxation rates—Sec. F; and the calculation of relaxation rates—Sec. G.

A. Electronic structure

The electronic structure of electrons in a SL is found from the solution of the 8×8 EFA (envelope function Hamiltonian).[25] The SL consists of alternating layers of InAs having width $2a$ and GaSb having width $2b$, with the period $\ell = 2a + 2b$. For energies near the band gap edges, the carrier wave function can be approximated by a linear combination of the wave functions of the nearest bands—the conduction (C), heavy-hole (H), light-hole (L), and spin-orbit bands (SO)—in each material, with remote bands included via the Löwdin perturbation scheme.[25] Explicitly, let $\mathbf{r}_{||} = (x,y)$ be the in-plane coordinate and z point in the direction of the SL axis. The energy bands and wave functions are functions of the wave vector $\mathbf{k} = (\mathbf{k}_{||},k_z)$, where $\mathbf{k}_{||}$ is the transverse wave vector, and the perpendicular wave vector $-\pi/\ell < k_z \leqslant \pi/\ell$ spans the Brillouin zone in the growth direction. Overall the envelope wave function for the explicitly included components is written as

$$\langle \mathbf{r}_{||},z \mid \mathbf{k}_{||},k_z\rangle = \psi_{\mathbf{k}}(\mathbf{r}_{||},z) = \frac{1}{\sqrt{A}}\exp(i\mathbf{k}_{||}\bullet\mathbf{r}_{||}) \times \sum_{n=1}^{8} c_n\phi_n(k_z,z), \tag{1}$$

comprising a plane wave in the in-plane direction and a linear combination of the eight-envelope functions $\phi_n(k_z,z)$ in the growth direction. Imposition of the usual boundary conditions gives rise to a secular equation for energies, $E(\mathbf{k}_{||},k_z)$, and wave functions, $\{\phi_n(k_z,z),n = 1\ldots 8\}$, in the 8×8 envelope-function approximation.

However, for the system of interest here, this level of rigor is unnecessary since the calculated energy spectra can be well approximated by the decoupled sum[26]

$$E(\mathbf{k}_{||},k_z) = \frac{\hbar^2 k_{||}^2}{2m_{||}} + \varepsilon(k_z), \tag{2}$$

where $m_{||}$ is the effective mass in the in-plane direction and $\varepsilon(k_z)$ is the dispersion in the growth direction. So, in order to make use of this decoupling and to speed up the transport calculation, the problem is simplified by breaking it into two parts. First the effective mass is found by solving the full 8×8 EFA[26] at $k_z = 0$ for $E(\mathbf{k}_{||},k_z = 0)$ and fitting a parabola to the calculated band. The parabolic approximation holds very well several tens of meV above the bottom of the conduction band.

The band dispersions $\varepsilon(k_z)$ in the growth direction are calculated by first setting $\mathbf{k}_{||} = 0$ and neglecting the far-off bands, which decouples the 8×8 EFA Hamiltonian into two identical 4×4 Hamiltonians.[25] In turn each 4×4 Hamiltonian splits into a 1×1 problem for the heavy holes and a 3×3 Hamiltonian that couples the C, LH, and SO bands.[27] The 3×3 coupled EFA Hamiltonian reads

$$\begin{pmatrix} V_C(z) & \Pi\sqrt{\frac{2}{3}}p_z & \frac{i\Pi p_z}{\sqrt{3}} \\ \Pi\sqrt{\frac{2}{3}}p_z & V_{LH}(z) & \frac{i\Delta E}{\sqrt{2}} \\ -\frac{i\Pi p_z}{\sqrt{3}} & -\frac{i\Delta E}{\sqrt{2}} & V_{SO}(z) \end{pmatrix} \begin{pmatrix} \phi_C(z) \\ \phi_{LH}(z) \\ \phi_{SO}(z) \end{pmatrix} = \varepsilon(k_z) \begin{pmatrix} \phi_C(z) \\ \phi_{LH}(z) \\ \phi_{SO}(z) \end{pmatrix}, \tag{3}$$

where $p_z = -i\hbar(d/dz)$ is the momentum operator; $\Pi = -i\langle s|p_x|x\rangle/m_0$ is the Kane momentum matrix element with $E_P = 2m_0\Pi^2$; $V_C(z)$, $V_{LH}(z)$, and $V_{SO}(z)$ denote the appropriate strain-dependent, bulk-band edges; and $\varphi_C(z)$, $\varphi_{LH}(z)$, and $\varphi_{SO}(z)$ are the envelope-function components. In terms of perpendicular and horizontal strains, $\varepsilon_\perp$ and $\varepsilon_{||}$, and the deformation potentials b, the heavy-light band splitting for (001) growth is $\Delta E = 2b(\varepsilon_\perp - \varepsilon_{||})$.[8,23] In response to strains the Kane element changes to $\Pi = \Pi^{(0)}(1-\varepsilon_\perp)$, and the band edges shift as follows.[27]

$$V_{HH} = V_{HH}^{(0)} + a_V\frac{\Delta\Omega}{\Omega} - \frac{1}{2}\Delta E, \tag{4}$$

$$V_{LH} = V_{LH}^{(0)} + a_V\frac{\Delta\Omega}{\Omega} + \frac{1}{2}\Delta E, \tag{5}$$

$$V_C = V_C^{(0)} + a_C\frac{\Delta\Omega}{\Omega}, \tag{6}$$

$$V_{SO} = V_{SO}^{(0)} + a_V\frac{\Delta\Omega}{\Omega}, \tag{7}$$

where $\Delta\Omega/\Omega = 2\varepsilon_{||} + \varepsilon_\perp$; a_C and a_V are the hydrostatic conduction and valence band deformation potentials, respectively; Δ_0 is the spin-orbit splitting; and $V^{(0)}$ and $\Pi^{(0)}$ denote the unstrained band edges and the Kane matrix element in the absence of strain, respectively. The InAs/GaSb band overlap—the difference between the valence-band edge of GaSb and the conduction-band edge of InAs, is taken to be 150 meV.[27] The input data used in the model is provided in Table I, using data from the model solid theory of Van de Walle[28] and Landölt-Borstein tables[29]; Kane parameters Π are from Bastard.[25]

Equation (3) can be simplified further to yield a Schrödinger-like equation[27]

$$\left[-\frac{\hbar^2}{2}\frac{d}{dz}\frac{1}{m(z)}\frac{d}{dz} + V_C(z)\right]\phi_C(z) = \varepsilon(k_z)\phi_C(z), \tag{8}$$

with an "effective" C/LH/SO mass $m(z)$ defined by

$$m(z) = \frac{3[\Delta E^2/2 - (V_{LH}(z)-\varepsilon)(V_{SO}(z)-\varepsilon)]}{2\Pi^2[2(V_{SO}(z)-\Delta E-\varepsilon)+V_{LH}(z)-\varepsilon]}, \tag{9}$$

with the other two components of the envelope wave function given by,

$$\phi_{LH}(z) = \frac{\hbar}{i}\left(\sqrt{\frac{2}{3}}\frac{2(V_{SO}(z)-\varepsilon)-\Delta E}{\Delta E^2 - 2(V_{LH}(z)-\varepsilon)(V_{SO}(z)-\varepsilon)}\right) \times \Pi\frac{d\phi_C(z)}{dz}, \tag{10}$$

TABLE I. Material parameters for the model calculation.

	E_C (meV)	E_V (meV)	E_{SO} (meV)	γ_1	γ_2	γ_3
InAs	0	−410	−790	−19.67	−8.37	−9.29
GaSb	960	157	−663	−11.80	−4.03	−5.26
	a_0(Å)	$C_{11}(10^{11}$ dyncm$^{-2})$		$C_{12}(10^{11}$ dyncm$^{-2})$		$C_{44}(10^{11}$ dyncm$^{-2})$
InAs	6.0584	8.33		4.53		3.96
GaSb	6.0954	9.08		4.13		4.45
	Π^2(eV)	a_V(eV)	a_C(eV)	b(eV)		d(eV)
InAs	21.11	1.0	−5.08	−1.80		−3.60
GaSb	22.88	0.79	−6.85	−2.00		−4.80

$$\phi_{SO}(z) = \hbar \frac{\Delta E - (V_{LH} - \varepsilon)}{(\Delta E)^2 - 2(V_{LH} - \varepsilon)(V_{SO} - \varepsilon)} \frac{2\Pi}{\sqrt{3}} \frac{d\phi_C(z)}{dz}. \tag{11}$$

The effective masses $m(z)$ [Eq. (9)] in both materials are shown in Fig. 1.

In Fig. 1 the effective mass is strongly energy dependent: for example, for GaSb the mass becomes negative (light-hole like) below the valence-band edge of GaSb. Clearly it is inaccurate to use bulk band-edge masses in effective-mass like calculations far away from band edges. Because of tensile strain in InAs, the bottom of the conduction band in InAs extends slightly below the bottom of the conduction band in bulk InAs.

The Schrodinger equation for the SL is solved subject to the usual periodic boundary conditions. In the flat-band case the envelope function solutions are exponentials of the form[25]

$$\phi_C^A(z) = C_1 e^{ik_A z} + C_2 e^{-ik_A z} \quad -a \leqslant z \leqslant a, \tag{12}$$

$$\phi_C^B(z) = C_3 e^{ik_B z} + C_4 e^{-ik_B z} \quad a \leqslant z \leqslant a + 2b, \tag{13}$$

where

$$k_{A,B} = \left[2m_{A,B}\left(\varepsilon - V_C(z)\right)/\hbar^2\right]^{1/2}, \tag{14}$$

with A = InAs and B = GaSb (Fig. 1). The boundary conditions on the continuity of the envelope function ϕ_C and its derivative $\frac{1}{m(z)}\frac{d\phi_C}{dz}$, together with the Bloch condition, yield the secular equation

$$\begin{pmatrix} e^{ik_A a} & e^{-ik_A a} & -e^{ik_B a} & -e^{-ik_B a} \\ \frac{k_A}{m_A} e^{ik_A a} & -\frac{k_A}{m_A} e^{-ik_A a} & -\frac{k_B}{m_B} e^{ik_B a} & \frac{k_B}{m_B} e^{-ik_B a} \\ e^{-ik_A a} & e^{ik_A a} & -e^{-iqd} e^{ik_B(a+2b)} & -e^{-iqd} e^{-ik_B(a+2b)} \\ \frac{k_A}{m_A} e^{-ik_A a} & -\frac{k_A}{m_A} e^{ik_A a} & -e^{-iqd}\frac{k_B}{m_B} e^{ik_B(a+2b)} & e^{-iqd}\frac{k_B}{m_B} e^{-ik_B(a+2b)} \end{pmatrix} \begin{pmatrix} C_1 \\ C_2 \\ C_3 \\ C_4 \end{pmatrix} = 0 \tag{15}$$

for the wave function and the Kronig-Penney (KP) equation for the energy eigenvalues,[25]

$$\cos k_z d = \cos k_A L_A \cos k_B L_B - \tfrac{1}{2}(\eta + \eta^{-1}) \times \sin k_A L_A \sin k_B L_B, \tag{16}$$

where $\eta = \frac{k_A m_B}{k_B m_A}$. At the level of approximation of the 3×3 Hamiltonian, the LH and SO components of the wave function are not continuous.[30]

As an example, Fig. 2 shows several calculated band structures for SLs with layer widths 20Å InAs/40Å GaSb, 20Å InAs/20Å GaSb, and 40Å InAs/20Å GaSb that span all three short (SW)-, mid (MW)-, and long (LW)-wavelength infrared (IR) detection windows, respectively. As expected, the narrower the InAs-layer width, the higher the band centroid, and the wider the period, the narrower the bandwidth. Owing to the band nonparabolicity evident in Fig. 1, the higher the band, the heavier the carrier effective mass; the calculated numbers for the SWIR, MWIR, and LWIR SLs in Fig. 2 are $0.0396m_0$, $0.0297m_0$, and $0.0254m_0$, respectively. Importantly, a one-monolayer variation of InAs-layer width changes the calculated bandwidth only by about 7% for the cases in Fig. 1, which justifies our use of the Boltzmann equation approach. For typical values of doping (10^{10} cm^{-2} per period), the Fermi levels are on the order of 5–30 meV, which translates into Fermi wave vectors on the order of a few tenths of the Brillouin zone size. Therefore, electrons occupy only the ground-state subband near the bottom of the band.

Once the eigenvalues of the KP equation [Eq. (16)] are located, the wave function amplitudes (C_1, C_2, C_3, C_4) are found from (15). The corresponding light- and spin-orbit amplitudes (L_1, L_2, L_3, L_4) and (S_1, S_2, S_3, S_4) are calculated from Eqs. (10) and (11), and then the wave function normalized

as(a) $\varepsilon \geqslant V_{\mathrm{LH}}(GaSb)$, $k_B = i\kappa_B$

$$2a(C_1C_1^* + L_1L_1^* + S_1S_1^* + C_2C_2^* + L_2L_2^* + S_2S_2^*) + 2b(C_3C_4^* + L_3L_4^* + S_3S_4^* + C_4C_3^* + L_4L_3^* + S_4S_3^*) + \\ + (C_1C_2^* + L_1L_2^* + S_1S_2^* + C_2C_1^* + L_2L_1^* + S_2S_1^*)\sin 2k_Aa/k_A \\ + [(C_3C_3^* + L_3L_3^* + S_3S_3^*)e^{-\kappa_Bd} + (C_4C_4^* + L_4L_4^* + S_4S_4^*)e^{\kappa_Bd}]\sinh 2\kappa_Bb/\kappa_B = 1 \quad (17a)$$

and (b) $\varepsilon < V_{\mathrm{LH}}(\mathrm{GaSb})$

$$2a(C_1C_1^* + L_1L_1^* + S_1S_1^* + C_2C_2^* + L_2L_2^* + S_2S_2^*) + 2b(C_3C_3^* + L_3L_3^* + S_3S_3^* + C_4C_4^* + L_4L_4^* + S_4S_4^*) \\ + (C_1C_2^* + L_1L_2^* + S_1S_2^* + C_2C_1^* + L_2L_1^* + S_2S_1^*)\sin 2k_Aa/k_A \\ + [(C_3C_4^* + L_3L_4^* + S_3S_4^*)e^{ik_Bd} + (C_4C_3^* + L_4L_3^* + S_4S_3^*)e^{-ik_Bd}]\sin 2k_Bb/k_B = 1. \quad (17b)$$

In the case of IRS the scattering rates depend on the modulus of the carrier-wave function at the interfaces [see Eqs. (24), (39), and (40) later in the text]. For the three SLs of Fig. 2 the moduli of the wave function at the interfaces are shown in Fig. 3.

Figure 3 may be understood as follows. The wave function for the ground state subband at $k_z = 0$ is symmetric with respect to the reflection across the midpoint $z = 0$ of the InAs layer and across the midpoint $z = a + b$ of the GaSb layer; at $k_z = \pi/d$ the wave function is symmetric about $z = 0$ but antisymmetric about $z = a + b$, which is, therefore, a node. Hence, the value of $|\phi_{k_z}(a)|^2$ must decrease as a function of k_z from $k_z = 0$ to $k_z = \pi/d$, as it does in Fig. 3. For the model SLs the LH/SO components of the wave function account for less than 7% of the total normalization.

B. Scattering mechanism

Interface roughness in the form of monolayer fluctuations has been shown to be the main source of carrier scattering in SLs, affecting horizontal transport in SLs up to almost the room temperature, where polar-optical phonon scattering becomes dominant.[31] The characteristic signature of IRS is a strong power dependence of mobility on layer width. Indeed, in the quantum-well limit, Gold's theory predicts that mobility depends on the sixth power of layer width.[32]

The fluctuation of the interface position at a point $\mathbf{r}_{||}$ is characterized by height $\Delta(\mathbf{r}_{||})$ and by the lateral correlation length of interface fluctuations Λ.[33] The fluctuation gives rise to a perturbation potential at each interface

$$\delta V(\mathbf{r}_{||},z) = V_0[\theta(z - a - \Delta'(\mathbf{r}_{||})) - \theta(z - a)] \\ + V_0[\theta(-z + a + \Delta(\mathbf{r}_{||})) - \theta(-z + a)], \quad (18)$$

with the magnitude V_0 (given by the height of the InAs conduction well) and localized at the well/barrier $z = a$ and barrier/well interfaces $z = -a$, respectively. To first order in the fluctuation, the Taylor expansion of the perturbation yields[33]

$$\delta V(\mathbf{r}_{||},z) = -V_0\Delta'(\mathbf{r}_{||})\delta(z - a) + V_0\Delta(\mathbf{r}_{||})\delta(z + a), \quad (19)$$

where the fluctuations $\Delta'(\mathbf{r}_{||})$ and $\Delta(\mathbf{r}_{||})$ are considered uncorrelated.

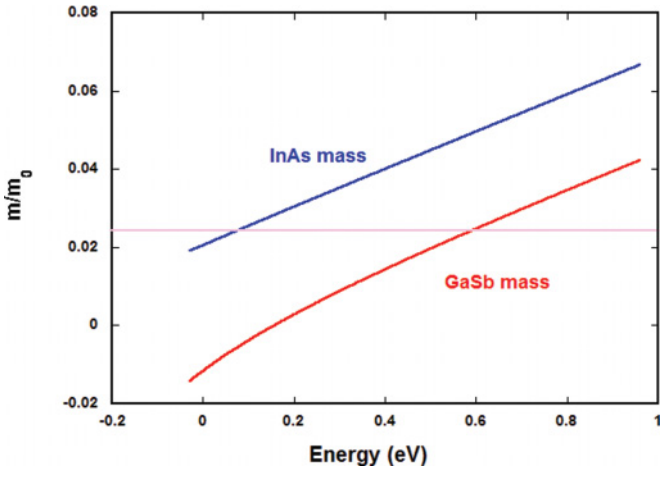

FIG. 1. (Color online) The bulk "effective" C/LH/SO mass $m(z)$ Eq. ((9)) in the well (InAs) and barrier (GaSb) materials as a function of energy. The horizontal line is at the value of $0.024m_0$ that is appropriate at the conduction band edge of bulk InAs. The zero of energy is at the bottom of the conduction band of unstrained InAs. The strain conditions are those for a 20Å InAs/20Å GaSb SL grown on a GaSb substrate.

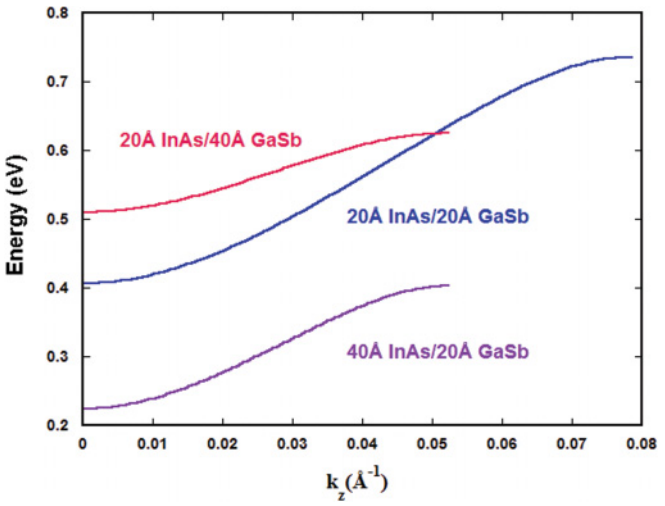

FIG. 2. (Color online) Electron energy bands along the growth direction for three combinations of InAs/GaSb layer widths. For typical carrier densities, at low temperatures, the Fermi energies are approximately 5–30 meV.

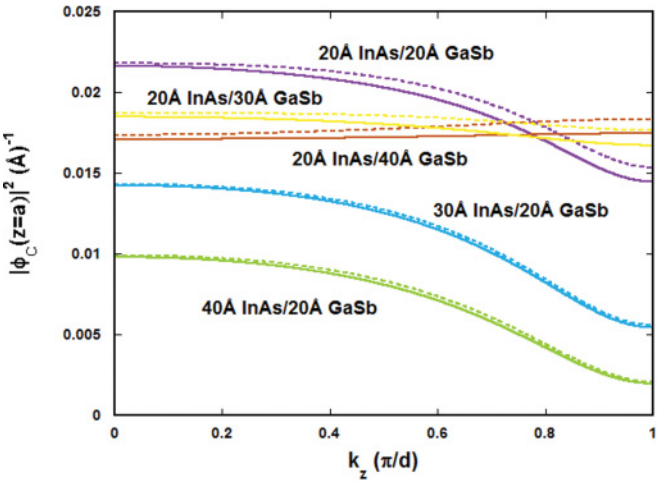

FIG. 3. (Color online) The modulus squared of the electron wave function at SL interfaces $|\phi_C(a)|^2$ for several combinations of layer widths as a function of the Brillouin zone wave vector in the growth direction (the continuous curve). Without the light- and spin-orbit wave function components, one obtains the dashed curves.

The autocorrelation function of interface fluctuations is assumed to be Gaussian[33] with the ensemble average

$$\langle \Delta(\mathbf{r}_{||})\Delta(\mathbf{r}'_{||})\rangle = \Delta^2 \exp(-|\mathbf{r}_{||} - \mathbf{r}'_{||}|^2/\Lambda^2), \tag{20}$$

and spectral density

$$S(q) = \pi \Delta^2 \Lambda^2 \exp(-\Lambda^2 q^2/4). \tag{21}$$

C. Scattering rates

The transition rate for IR-induced scattering between eigenstates $\psi_{\mathbf{k}}(\mathbf{r}_{||},z)$ and $\psi_{\mathbf{k}'}(\mathbf{r}_{||},z)$ of the SL from Fermi's Golden Theorem is given by[34]

$$T(\mathbf{k},\mathbf{k}') = \frac{2\pi}{\hbar}|M(\mathbf{k},\mathbf{k}')|^2 \delta(E(\mathbf{k}) - E(\mathbf{k}')), \tag{22}$$

where the square of transition matrix $M(\mathbf{k},\mathbf{k}')$ is

$$|M(\mathbf{k},\mathbf{k}')|^2 = |\langle \mathbf{k}_{||},k_z|\delta V(\mathbf{r}_{||})|\mathbf{k}'_{||},k'_z\rangle|^2. \tag{23}$$

The ensemble-averaged transition matrix is found to be

$$\frac{V_0^2}{A^2}\int \exp(i(\mathbf{k}'_{||} - \mathbf{k}_{||}) \bullet (\mathbf{r}_{||} - \mathbf{r}'_{||})) \times [\langle\langle \Delta'(\mathbf{r}_{||})\Delta'(\mathbf{r}'_{||})\rangle\rangle |\phi_{k_z}(a)|^2|\phi_{k'_z}(a)|^2 + \langle\langle \Delta(\mathbf{r}_{||})\Delta(\mathbf{r}'_{||})\rangle\rangle |\phi_{k_z}(-a)|^2|\phi_{k'_z}(-a)|^2] d\mathbf{r}_{||}d\mathbf{r}'_{||},$$

where $\langle\langle \Delta(\mathbf{r}_{||})\Delta(\mathbf{r}'_{||})\rangle\rangle$ is the ensemble average of roughness along the $z = -a$ interface and $\langle\langle \Delta'(\mathbf{r}_{||})\Delta'(\mathbf{r}'_{||})\rangle\rangle$ for the $z = a$ interface, the cross-terms vanishing because of no cross-correlation between the interfaces. Using the Gaussian autocorrelation function, the transition rate becomes

$$T(\mathbf{k},\mathbf{k}') = \frac{2\pi}{\hbar}\frac{\pi V_0^2}{A}\{\Delta'^2\Lambda'^2 \exp(-|\mathbf{k}_{||} - \mathbf{k}'_{||}|^2\Lambda'^2/4)|\phi_{k'_z}(a)|^2 \times |\phi_{k_z}(a)|^2 + \Delta^2\Lambda^2 \exp(-|\mathbf{k}_{||} - \mathbf{k}'_{||}|^2\Lambda^2/4) \times |\phi_{k'_z}(-a)|^2|\phi_{k_z}(-a)|^2\}\, \delta(E(\mathbf{k}) - E(\mathbf{k}')).$$

In the present paper the potential is symmetric (hence the wave-function moduli at $z = \pm a$ are equal), and the interfaces are assumed to be characterized by the same degree of roughness, $\Delta = \Delta'$, hence[21]

$$T(\mathbf{k},\mathbf{k}') = 2 \times \frac{2\pi}{\hbar}\left\{\frac{V_0^2\pi\Delta^2\Lambda^2}{A}\exp(-|\mathbf{k}_{||} - \mathbf{k}'_{||}|^2\Lambda^2/4) \times |\phi_{k_z}(a)|^2|\phi_{k'_z}(a)|^2\right\}\delta(E(\mathbf{k}) - E(\mathbf{k}')). \tag{24}$$

Since $|\phi_{k'_z}(a)|^2 = |\phi_{-k'_z}(a)|^2$, the scattering is randomizing,[34] $T(\mathbf{k}_{||},k_z;\mathbf{k}'_{||},-k'_z) = T(\mathbf{k}_{||},k_z;\mathbf{k}'_{||},k'_z)$. The randomizing property is quite general, depending only on the fact that the autocorrelation function of interface roughness does not depend on the vertical coordinate.

D. Boltzmann equation

When the conduction band is wide, electron motion is diffusive and can be described with the Boltzmann transport equation for the electron distribution function $f(\mathbf{k})$.[34] In the steady state the Boltzmann equation reads[35]

$$\left.\frac{\partial f}{\partial t}\right|_c = e\mathbf{F} \bullet \frac{1}{\hbar}\frac{\partial f}{\partial \mathbf{k}}, \tag{25}$$

where electron acceleration by the applied electric field $\mathbf{F}$ is counterbalanced by electron scattering. The scattering term is given by the integral[34,35]

$$\left.\frac{\partial f}{\partial t}\right|_c = -\frac{V}{(2\pi)^3}\int [T(\mathbf{k},\mathbf{k}')f(\mathbf{k})(1 - f(\mathbf{k}')) - T(\mathbf{k}',\mathbf{k})(1 - f(\mathbf{k}))f(\mathbf{k}')]d\mathbf{k}', \tag{26}$$

where the first/second terms correspond to out- and in-scattering. In an applied electric field $\mathbf{F}$ the electron-distribution function can be written as

$$f = f_0 + g, \tag{27}$$

where f_0 is the equilibrium Fermi-Dirac distribution function $f_0 = [1 + \exp((E - E_F)/kT)]^{-1}$. In the ohmic regime the departure from equilibrium g is expanded to first power in the applied field[34,35]

$$g(\mathbf{k}) = \tau(\mathbf{k})\frac{e}{\hbar}\left(\mathbf{F} \bullet \frac{\partial E}{\partial \mathbf{k}}\right)\frac{\partial f_0}{\partial E} \tag{29}$$

in terms of the unknown relaxation time $\tau(\mathbf{k})$.

The relaxation times are derived by using the microscopic reversibility condition,

$$T(\mathbf{k}',\mathbf{k}) = T(\mathbf{k},\mathbf{k}')\frac{f_0(\mathbf{k})(1 - f_0(\mathbf{k}'))}{f_0(\mathbf{k}')(1 - f_0(\mathbf{k}))} \tag{30}$$

and inserting the distribution function [Eq. (29)] into the Boltzmann equation [Eq. (26)], which yields the defining equation

$$\frac{V}{(2\pi)^3}\int d\mathbf{k}'T(\mathbf{k},\mathbf{k}')\frac{1 - f_0(\mathbf{k}')}{1 - f_0(\mathbf{k})} \times \left[g(\mathbf{k}) - \frac{f_0(\mathbf{k})(1 - f_0(\mathbf{k}))}{f_0(\mathbf{k}')(1 - f_0(\mathbf{k}'))}g(\mathbf{k}')\right] \equiv \frac{g(\mathbf{k})}{\tau(\mathbf{k})}. \tag{31}$$

Hence, in general, the relaxation time is given by[34,35]

$$\frac{1}{\tau(\mathbf{k})} = \frac{V}{(2\pi)^3}\int d\mathbf{k}' T(\mathbf{k},\mathbf{k}')\frac{1-f_0(\mathbf{k}')}{1-f_0(\mathbf{k})} \times\left[1-\frac{f_0(\mathbf{k})(1-f_0(\mathbf{k}))}{f_0(\mathbf{k}')(1-f_0(\mathbf{k}'))}\frac{g(\mathbf{k}')}{g(\mathbf{k})}\right]. \quad (32)$$

1. In-plane relaxation rate

For the field orientation along the x-axis,

$$g(\mathbf{k}) = \tau_{||}(\mathbf{k})eF_x\frac{\partial f_0}{\partial E}\left(\frac{1}{\hbar}\frac{\partial E}{\partial k_x}\right) = \tau_{||}(\mathbf{k})eF_x\frac{f_0(1-f_0)}{kT}\left(\frac{1}{\hbar}\frac{\partial E}{\partial k_x}\right), \quad (33)$$

hence assuming an isotropic-parabolic in-plane band dispersion,[34,35]

$$\frac{1}{\tau_{||}(\mathbf{k})} = \frac{V}{(2\pi)^3}\int d\mathbf{k}' T(\mathbf{k},\mathbf{k}')\frac{1-f_0(\mathbf{k}')}{1-f_0(\mathbf{k})} \times\left[1-\frac{\tau_{||}(\mathbf{k}')k'_{||}\cos\varphi'}{\tau_{||}(\mathbf{k})k_{||}\cos\varphi}\right], \quad (34)$$

where the angles between the field direction and wave vectors $(\mathbf{k}_{||},\mathbf{k}'_{||})$ are (φ,φ'), respectively.

Since $\cos\varphi' = \cos(\varphi+\theta) = \cos\varphi\cos\theta - \sin\varphi\sin\theta$, where θ is the angle between vectors $(\mathbf{k}_{||},\mathbf{k}'_{||})$, finally

$$\frac{1}{\tau_{||}(\mathbf{k})} = \frac{V}{(2\pi)^3}\int d\mathbf{k}'\left[1-\frac{k'_{||}}{k_{||}}\frac{\tau_{||}(\mathbf{k}')}{\tau_{||}(\mathbf{k})}\cos\theta\right] \times\frac{1-f_0(\mathbf{k}')}{1-f_0(\mathbf{k})}T(\mathbf{k},\mathbf{k}'), \quad (35)$$

since the $\sin\theta$ term drops out due to parity considerations. Since IRS is elastic, $f_0(\mathbf{k}') = f_0(\mathbf{k})$, the relaxation time becomes[36]

$$\frac{1}{\tau_{||}(k_r,k_z)} = \frac{V}{(2\pi)^3}\int\left[1-\frac{k'_r}{k_r}\frac{\tau_{||}(k'_r,k'_z)}{\tau_{||}(k_r,k_z)}\cos\theta\right] \times T(k_r,k_z;k'_r,k'_z;\theta)k'_r dk'_r dk'_z d\theta, \quad (36)$$

where $k_r = |\mathbf{k}_{||}|$.

2. Vertical relaxation rate

For the field applied in the z-direction, one similarly has

$$\frac{1}{\tau_\perp(\mathbf{k})} = \frac{V}{(2\pi)^3}\int d\mathbf{k}'\left[1-\frac{\tau_\perp(\mathbf{k}')\left(\frac{\partial E}{\partial k'_z}\right)}{\tau_\perp(\mathbf{k})\left(\frac{\partial E}{\partial k_z}\right)}\right]T(\mathbf{k},\mathbf{k}'); \quad (37)$$

however, owing to randomization, the scattering rate is even in k'_z while $\partial E/\partial k'_z$ is odd, so that the in-scattering term integrates to zero, hence[34,35]

$$\frac{1}{\tau_\perp(k_r,k_z)} = \frac{V}{(2\pi)^3}\int T\left(\mathbf{k},\mathbf{k}'\right)d\mathbf{k}'_{||}dk'_z = \frac{V}{(2\pi)^3}\int T\left(k_r,k_z;k'_r,k'_z;\theta\right)k'_r dk'_r dk'_z d\theta. \quad (38)$$

E. Expressions for IRS relaxation rates

1. Vertical relaxation rates

Using Eq. (24) for the scattering rates, the integration over the in-plane coordinates $k'_r dk'_r d\theta'$ can be performed analytically, yielding[23]

$$\frac{1}{\tau_\perp(E,k_z)} = 2\times\left(\frac{m_{||}\ell}{\hbar^3}V_0^2|\phi_{k_z}(a)|^2\right)\Omega^2\Lambda^2 \times\left\{\int_0^{\pi/l}dk'_z|\phi_{k'_z}(a)|^2 I_0\left(\frac{\Lambda^2 k'_r k_r}{2}\right) \times\exp\left(-\frac{\Lambda^2}{4}\left(k'^2_r+k^2_r\right)\right)\Theta\left(E-\varepsilon\left(k'_z\right)\right)\right\}, \quad (39)$$

where I_0 is the zeroth-order,[37] modified Bessel function of the first kind, $k_r = |\mathbf{k}_{||}|$, and Θ is the Heaviside step function.

2. Horizontal relaxation rates

Similarly for the horizontal relaxation rates [Eq. (36)], one must also integrate the in-scattering term containing $\cos\theta\prime$, and we derive the following expression,

$$\frac{1}{\tau_{||}(E,k_z)} = 2\times\left(\frac{m_{||}\ell}{\hbar^3}V_0^2|\phi_{k_z}(a)|^2\right)\Omega^2\Lambda^2 \times\left\{\int_0^{\pi/l}dk'_z|\phi_{k'_z}(a)|^2\left[I_0\left(\frac{\Lambda^2 k'_r k_r}{2}\right) -\frac{k'_r}{k_r}\frac{\tau_{||}(E,k'_z)}{\tau_{||}(E,k_z)}I_1\left(\frac{\Lambda^2 k'_r k_r}{2}\right)\right] \times\exp\left(-\frac{\Lambda^2}{4}\left(k'^2_r+k^2_r\right)\right)\Theta\left(E-\varepsilon\left(k'_z\right)\right)\right\}, \quad (40)$$

where I_1 is the first-order, modified Bessel function of the first kind.[37] Its properties are

$$I_0(x) > I_1(x) \geqslant 0,$$

with the asymptotic values for small x,

$$I_0(x) \approx 1+(x/2)^2+\cdots \text{ and } I_1(x) \approx x/2+\cdots,$$

and for large values

$$I_0(x) \approx e^x/\sqrt{2\pi x}\left(1+\frac{1}{8x}+\cdots\right) \text{ and } I_1(x) \approx e^x/\sqrt{2\pi x}\left(1-\frac{3}{8x}+\cdots\right),$$

hence $I_1(x)$ approaches $I_0(x)$ asymptotically from below.

In the limit of very large Λ, one can use the asymptotic expressions and the fact that

$$\lim_{\Lambda\to\infty}\frac{\Lambda}{2\sqrt{\pi}}\exp\left(-\left(\frac{\Lambda}{2}\right)^2(k_r-k'_r)^2\right) = \delta(k_r-k'_r)\propto\delta(k_z\pm k'_z)$$

to show that $\tau_\perp^{-1}$ reaches an asymptotic value and $\tau_{||}^{-1}$ grows like Λ^{-2}. In this limit the scattering is purely specular.[23]

F. Mobilities

Mobilities $\boldsymbol{\mu}$ are found from the calculated current densities,[34,35]

$$\mathbf{j} = -en\boldsymbol{\mu} \bullet \mathbf{F} = -\frac{e}{4\pi^3}\int g(\mathbf{k})\mathbf{v}(\mathbf{k})d\mathbf{k} = -\frac{e}{4\pi^3}\int \tau(\mathbf{k})\frac{e}{\hbar}\left(\mathbf{F}\bullet\frac{\partial f_0}{\partial \mathbf{k}}\right)\mathbf{v}(\mathbf{k})d\mathbf{k}, \quad (41)$$

where velocity $\mathbf{v}(\mathbf{k}) = \frac{1}{\hbar}\frac{\partial E}{\partial \mathbf{k}}$ and carrier density $n = \frac{1}{4\pi^3}\int f_0(\mathbf{k})d\mathbf{k}$. Hence, the two mobilities are found from $\mu_{||} = j_{||}/enF_{||}$ and $\mu_\perp = j_z/enF_z$,

$$\mu_\perp = -e\frac{\int \tau_\perp(\mathbf{k})v_z^2\left(\frac{\partial f_0}{\partial E}\right)d\mathbf{k}}{\int f_0(\mathbf{k})d\mathbf{k}}, \quad (42)$$

$$\mu_{||} = -e\frac{\int \tau_{||}(\mathbf{k})v_{||}^2\left(\frac{\partial f_0}{\partial E}\right)d\mathbf{k}}{\int f_0(\mathbf{k})d\mathbf{k}}. \quad (43)$$

The calculation will be performed for temperatures near the absolute zero so that $\partial f_0/\partial E = -\delta(E - E_F)$. Since the relaxation rates themselves are temperature independent, an extension of the calculation to higher temperatures is straightforward, requiring only the replacement of the delta function $\delta(E - E_F)$ with $\partial f_0/\partial E = f_0(1 - f_0)/kT$ and the calculation of relaxation rates for energies within several kT of the chemical potential energy; the main challenge is numerical.

Specializing to the case of SLs with the energy band dispersion

$$E(\mathbf{k}) = E(k_r,k_z) = \frac{\hbar^2 k_r^2}{2m_{||}} + \varepsilon(k_z),$$

the carrier concentration is

$$n = \frac{1}{4\pi^3}\frac{2\pi m_{||}}{\hbar^2}\int_{-\pi/l}^{\pi/l}[E_F - \varepsilon(k_z)]\,dk_z, \quad (44)$$

and the areal density per period is simply $n\ell$. Similarly, the expressions for the mobilities are

$$\mu_\perp = \frac{1}{n}\frac{e}{2\pi^2\hbar^2}\int_{-\pi/l}^{\pi/l}\tau_\perp(E_F,k_z)\left[m_{||}\left(\frac{1}{\hbar}\frac{\partial E}{\partial k_z}\right)^2_{E=E_F}\right]dk_z, \quad (45)$$

$$\mu_{||} = \frac{1}{n}\frac{e}{2\pi^2\hbar^2}\int_{-\pi/l}^{\pi/l}\tau_{||}(E_F,k_z)[E_F - \varepsilon(k_z)]\,dk_z. \quad (46)$$

1. Theorem on mobilities

From Eqs. (39), and (40) the horizontal relaxation rates are seen to be smaller than the vertical rates, so that the relaxation times are related as

$$\tau_{||}(E,k_r) \geqslant \tau_\perp(E,k_r). \quad (47)$$

If these relaxation rates were weighted equally in Eqs. (42) and (43), then in absence of screening the IRS horizontal mobilities would be greater than the corresponding vertical mobilities $\mu_{||} \geqslant \mu_\perp$. However, equal weighting requires that the horizontal and vertical masses be equal, which may not hold for energies far from the conduction-band bottom.

G. Calculation of the relaxation rates

The relaxation rates are an intermediate result in the calculation and, as such, rarely examined. However, in order to understand the calculated mobilities, it is necessary to examine the behavior of the relaxation rates as a function of SL and roughness parameters. To this end, the IRS relaxation rates were calculated for a number of cases of interest.

1. Iteration experience

First we report on the iteration process used to solve the integral equation for the horizontal relaxation rates as it bears on the common approximations used to calculate the in-plane mobilities.

The iterative process is started with the solution in the quantum-well limit, for which $k_r' = k_r$, hence $\tau_{||}(E,k_r) = \tau_{||}(E,k_r')$, so the starting solution is

$$\frac{1}{\tau_{||}(E,k_z)} \propto \left\{\int_0^{\pi/l} dk_z'|\phi_{k_z'}(a)|^2 \left[I_0\left(\frac{\Lambda^2 k_r' k_r}{2}\right) - I_1\left(\frac{\Lambda^2 k_r' k_r}{2}\right)\right] \times \exp\left(-\frac{\Lambda^2}{4}\left(k_r'^2 + k_r^2\right)\right)\Theta(E - \varepsilon_z')\right\}. \quad (48)$$

The result is then inserted in Eq. (40) to continue the iteration process by adding a small fraction of the new result to the previous iteration until the results are converged to one part in a million. For $\Lambda^2 k_F^2/2 \ll 1$, $I_1(\Lambda^2 k_F^2/2) \ll I_0(\Lambda^2 k_F^2/2)$, so that the solution converges within a few iterations; for $\Lambda^2 k_F^2/2 \gg 1$, it can take a hundred iterations to achieve convergence. As an example, Fig. 4 shows the iteration experience for the indicated parameters.

The zeroth-order solution is seen to overestimate the final result, especially near the zone edge.

Nevertheless even with such cautious approach to self-consistency, the next several iterations produce nonphysical, negative relaxation rates in Fig. 4, which points to the failure of the nonself-consistent approximation,

$$\frac{1}{\tau_{||}(E,k_z)} \propto \left\{\int_0^{\pi/l} dk_z'|\phi_{k_z'}(a)|^2\left[I_0\left(\frac{\Lambda^2 k_r' k_r}{2}\right) - \frac{k_r'}{k_r}I_1\left(\frac{\Lambda^2 k_r' k_r}{2}\right)\right] \times \exp\left(-\frac{\Lambda^2}{4}\left(k_r'^2 + k_r^2\right)\right)\Theta\left(E - \varepsilon_z'\right)\right\}. \quad (49)$$

The final result in Fig. 4 is physical. Once self-consistency is achieved, however, further iterations can rapidly degrade the solution, leading to spurious oscillations owing to the round-off error.

2. Calculated unscreened relaxation rates

Here we examine the dependence of the relaxation rates on SL parameters. The simplest dependence is the proportionality

of the relaxation rates to the square of vertical roughness Δ, so that both mobilities are inversely proportional to Δ^2. In all cases examined, the vertical relaxation rates are greater than the horizontal rates, in agreement with the theorem derived previously.

Next we examine the dependence on doping and the correlation length. For typical values of residual doping,[38] the Fermi energy is much less than the bandwidth, hence the limit of the integration does not extend to the edge of the Brillouin zone. We distinguish two regimes: $\Lambda^2 k_F^2/2 \ll 1$ and $\Lambda^2 k_F^2/2 \gg 1$, cases (a) and (b) below.

(a) Small values, $\Lambda^2 k_F^2/2 \ll 1$.

For this case because the in-scattering term is small, there is a very small difference between the horizontal and vertical relaxation rates. Figure 5 shows the results for a 20Å InAs/40Å GaSb SL with $E_F = 25$ meV, $\Lambda = 30$Å, and $\Delta = 3$Å so that $\Lambda^2 k_F^2/2 = 0.071$. For small values of $x = \Lambda_i^2 k_F^2/2$, $I_0(x) \to 1$, $I_1(x) \to 0$, and $\exp(-x) \to 1$, so that for both mobilities

$$\frac{1}{\tau_\perp(E_F,k_z)} \approx \frac{1}{\tau_{||}(E_F,k_z)} \to |\phi_{k_z}(a)|^2 |\phi_{k_z=0}(a)|^2 \sqrt{E_F}. \quad (50)$$

Hence, the scattering rates are proportional to $\sqrt{E_F}$, the extent of the available phase space for scattering in the growth direction, and the curves in Fig. 5 are spaced as $\sqrt{E_F}$. Since the wave-function amplitudes are largely independent of k_z for small values of k_z (Fig. 3), the calculated relaxation rates (Fig. 5) are also relatively dispersionless.

(b) Large values, $\Lambda^2 k_F^2/2 \gg 1$.

For the parameters of Fig. 6 and $E_F = 25$ meV, $\Lambda_i^2 k_F^2/2 \approx 5.78$. The resulting dependence on the Fermi energies and vertical momentum is complex and best understood by examining the relaxation rates near the origin $k_z = 0$ and at the endpoint $k_z = k_{Fz}$, which are plotted in Fig. 7. In all cases even for large values of Λ, but small Fermi energies, the relaxation rates are proportional to $\sqrt{E_F}$ [Eq. (50)].

For larger Fermi energies, one can estimate the expected dependence as follows. Near the endpoint $k_z = k_{Fz}$ and $k_r = 0$, so that $I_0(0) = 1$. Since the modulus $|\phi_{k_z'}(a)|^2$ is a relatively slowly varying function, as seen in Fig. 3, the vertical relaxation rate will be proportional to

$$\frac{1}{\tau_\perp(E_F,k_{Fz})} \propto \exp(-\Lambda^2 m_{||} E_F/2) \int_0^{\pi/l} dk_z' \times \exp(\Lambda^2 m_{||} \varepsilon(k_z')/2) \Theta(E_F - \varepsilon(k_z')). \quad (51)$$

For the range of doping considered here, the range of integration is limited by the value of the Fermi wave vector in the z-direction, $\pi/l > k_{Fz} \propto \sqrt{E_F}$. Although the integral is nonanalytic, in the limit of large E_F it is proportional to $\exp(\Lambda^2 m_{||} E_F/\hbar^2)$, so that $\tau_\perp(E_F,k_{Fz})^{-1} \to$ constant, as reflected in Fig. 7. In the same limit the horizontal rates for k_{Fz} are found to decrease faster than the vertical rates because of the growing importance of the in-scattering term.

Near the origin $k_z = 0$ and $k_r = k_F$, and for large values of E_F, using the asymptotic expansion of the Bessel functions, the vertical rates can be shown to saturate

$$\tau_\perp(E_F,k_z = 0)^{-1} \to \text{constant},$$

and the horizontal rates to be inversely proportional to the Fermi energy

$$\tau_{||}(E_F,k_z = 0)^{-1} \to 1/E_F.$$

(c) Dependence on layer widths.

The present theory reduces properly to the quantum well limit, in which the scattering rates are proportional to the sixth power of layer width, here the width of the InAs layer. The analytic proof is given in Appendix A.

Figures 8 and 9 show the calculated dependence of the relaxation rates on layer width for two values of correlation length. For the short correlation length of $\Lambda = 30$ Å (Fig. 8), the vertical and horizontal scattering rates are practically indistinguishable because the in-scattering term is negligible. For barrier widths $2b = 24$, 38, 64 Å, the rates can be fitted to the power laws $\tau \propto a^{2.3}, a^{3.5}, a^{4.0}$, respectively, which

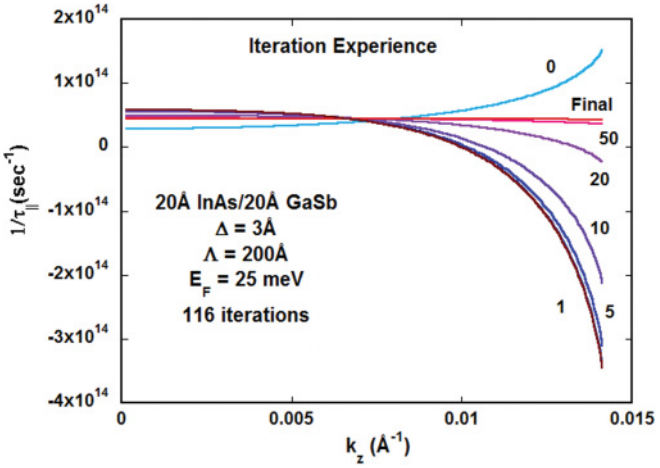

FIG. 4. (Color online) Iteration experience in solving the integral equation for the horizontal relaxation rates as a function of the iteration number and the Brillouin zone-wave vector. The graph highlights the inadequacy of the quantum-well approximation (zeroth iteration) and of the lack of self-consistency (first iteration).

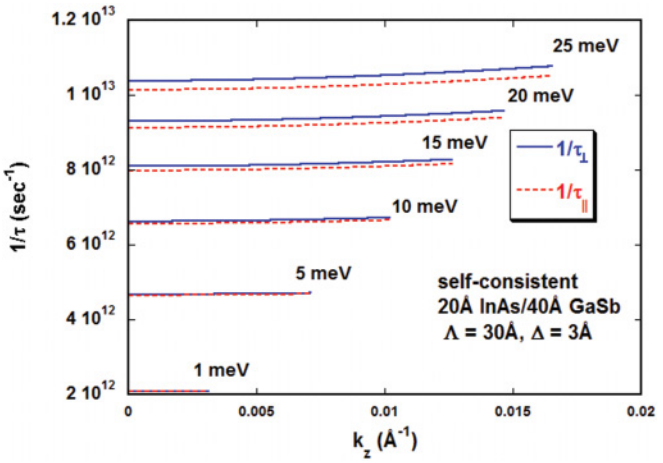

FIG. 5. (Color online) Calculated, self-consistent vertical and horizontal relaxation rates for a 20Å InAs/40Å GaSb SL with Λ = 30Å and Δ = 3Å, as a function of the Brillouin zone wave vector and Fermi energy. The curves terminate at the value of k_z, for which $E_F = \varepsilon(k_z)$.

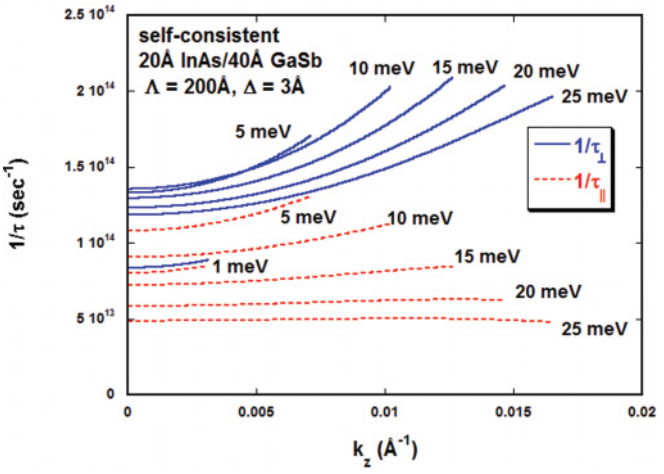

FIG. 6. (Color online) Calculated vertical and (self-consistent) horizontal relaxation rates for a 20Å InAs/40Å GaSb SL with $\Lambda = 200$Å and $\Delta = 3$Å, as a function of the Brillouin zone wave vector and Fermi energy.

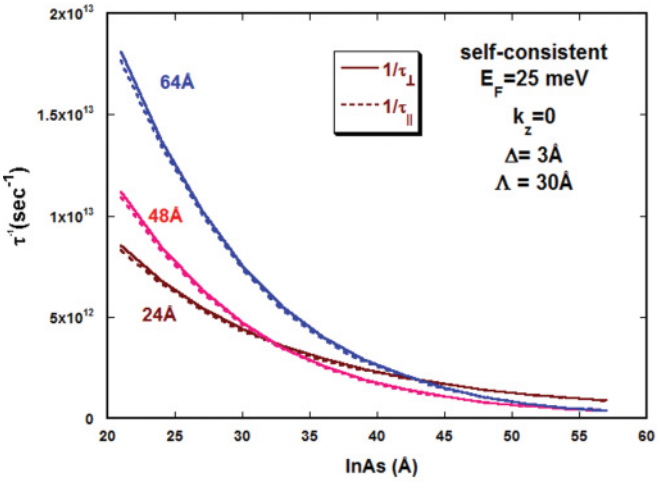

FIG. 8. (Color online) The calculated electron relaxation rates for several GaSb barrier widths as a function of InAs well width for a short correlation length: $\Lambda = 30$ Å, $E_F = 25$ meV, $\Delta = 3$Å, and $k_z = 0$.

approaches the quantum-well limit as InAs wells become more separated. Using only the data for InAs widths greater than 30 Å, the fitted power laws $\tau \propto a^{2.6}, a^{4.2}, a^{5.0}$ approach the quantum-well limit even closer.

For longer correlations lengths $\Lambda = 200$ Å (Fig. 9), the vertical ($\tau_\perp \propto a^{2.3}, a^{3.5}, a^{4.0}$) and horizontal ($\tau_{||} \propto a^{2.3}, a^{3.6}, a^{3.9}$) scattering rates differ markedly, but their power dependences are similar to each other and to those for the shorter correlation length (Fig. 8). Using only the data for InAs widths greater than 30 Å, the fits are $\tau_\perp \propto a^{2.6}, a^{4.2}, a^{5.0}$ and $\tau_{||} \propto a^{2.6}, a^{4.3}, a^{5.1}$. The similarity of these power laws underscores that the InAs-width dependence of the scattering rates derives primarily from the wave-function amplitudes.

III. CALCULATED MOBILITIES

A. Unscreened results

A number of mobility curves were calculated as a function of SL parameters, using converged relaxation rates. For this section only the parallel mass was fixed at $m_{||} = 0.024 m_0$. Figure 10 shows the calculated mobilities as a function of InAs-layer width for correlation lengths $\Lambda = 30$ and 200 Å and $E_F = 3$ meV. Since with increasing layer width the interface is an increasingly smaller fraction of the total width, the calculated mobilities increase with InAs-layer width, which is the hallmark of IRS.[32] For InAs widths greater than 60 Å, the conduction-band level falls below the top of the bulk-valence band in GaSb, so that the electron wave function no longer decays exponentially but oscillates in GaSb. In the 3×3 EFA model the transition from the decaying to oscillatory behavior inside the GaSb layer is smooth,[39] with mobilities rising at

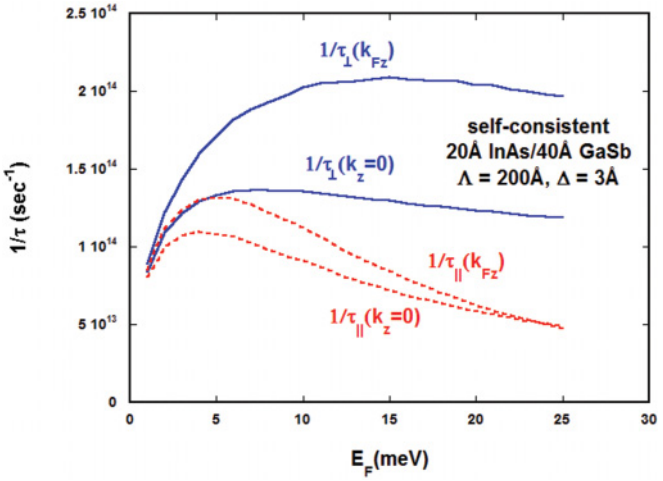

FIG. 7. (Color online) Calculated vertical and horizontal relaxation rates for a 20Å InAs/40Å GaSb SL with $\Lambda = 200$Å and $\Delta = 3$Å, as a function of Fermi energy near the center of the Brillouin zone and at the endpoint k_{Fz}.

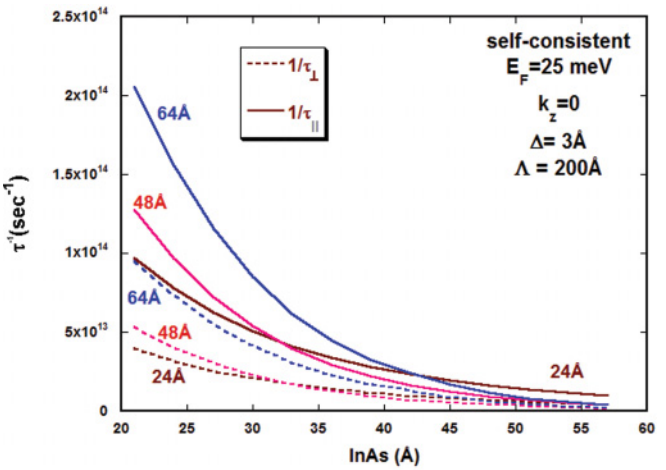

FIG. 9. (Color online) The calculated electron relaxation rates for several GaSb barrier widths as a function of InAs well width for a long correlation length: $\Lambda = 200$ Å, $E_F = 25$ meV, $\Delta = 3$Å, and $k_z = 0$.

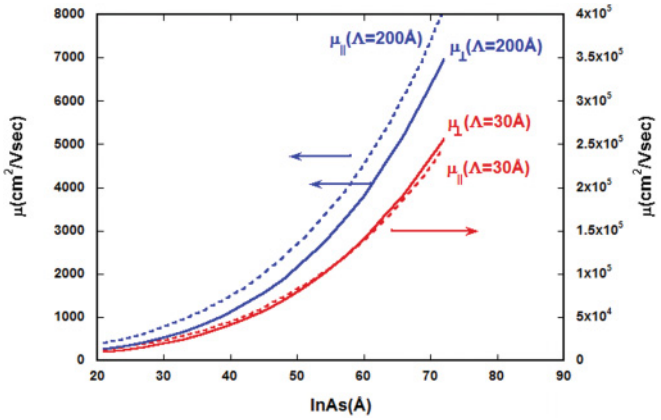

FIG. 10. (Color online) Calculated vertical and horizontal unscreened mobilities as a function of InAs-layer width for the indicated parameters; the parallel mass $m_{||} = 0.024m_0$.

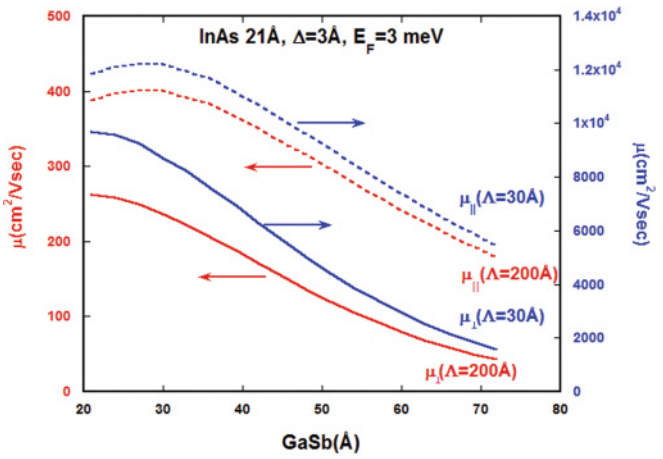

FIG. 11. (Color online) Calculated vertical and horizontal unscreened mobilities as a function of GaSb-layer width for the indicated parameters; parallel mass $m_{||} = 0.024m_0$.

an ever increasing rate as the InAs layer widens. For $\Lambda = 30$ Å the vertical mobilities become slightly larger than the horizontal mobilities because of the unequal weighting of the corresponding relaxation rates by the velocities in the mobility integral.

On the other hand the calculated mobilities decrease with GaSb layer width (Fig. 11) since the electron wave function cannot penetrate into the barrier material and so is more susceptible to InAs-layer width fluctuations.

B. Screened results

In this section we use the data for the four samples we studied earlier. The experimental sample parameters such as layer widths and horizontal mobilities are listed in Table II.[38] In addition we calculate the Fermi energies using the bands calculated with the 3×3 model, and the parallel masses and band gaps are calculated using the full 8×8 EFA model. Since we are dealing with *n*-type transport, we do not include the *p*-type sample, labeled as SL1 in Ref. 38, whose narrow width and measured low mobility led to the high-power dependence of mobility on layer width reported in Ref. 38. Its inclusion at the time was motivated by the fact that we were using Gold's theory that is appropriate to isolated quantum wells, which moreover does not distinguish between *n*- and *p*-type conduction and is independent of parallel mass. The challenging *p*-type transport merits an independent study.

For comparison with data it is necessary to take into account the electron screening of IRS. Here, we adapt the Thomas-Fermi form of screening, which requires that the transition matrix be multiplied by the screening factor[40]

$$S_C(q) = \left(\frac{q}{q+q_s}\right)^2 = \left(\frac{|\mathbf{k}_{||} - \mathbf{k}'_{||}|}{|\mathbf{k}_{||} - \mathbf{k}'_{||}| + q_s}\right)^2 = \left(\frac{\sqrt{k_r^2 - 2k_r k'_r \cos\theta' + k_r'^2}}{\sqrt{k_r^2 - 2k_r k'_r \cos\theta' + k_r'^2} + q_s}\right)^2, \quad (52)$$

where q_s is the Thomas-Fermi screening wave vector $q_s = \frac{m_{||}e^2}{2\pi\varepsilon\hbar^2}$ and ε is the bulk dielectric constant. For the numbers appropriate to InAs, the Thomas-Fermi screening length is about $q_s^{-1} \approx 180$ Å. Given the carrier densities in Table II, $(k_F)^{-1} \approx 200$Å, which is on the order of q_s^{-1}, so that electronic screening cannot be neglected. Inclusion of screening makes the angular integrals for the scattering rates nonanalytic.

The overall effect of screening is to reduce the scattering rates and enhance mobilities. However, the vertical and horizontal scattering rates are affected differently because of the angular dependence of $S_C(q)$. In fact the vertical rates are reduced more since screening is largest for backward scattering, $\theta' = \pi$, where $1 - (k'_r/k_r)\cos\theta' = 1 + (k'_r/k_r)$ so that horizontal rates are accentuated with

TABLE II. Data for the four samples in this study, including the experimental layer widths and horizontal low-temperature (10 K) mobilities, as well as calculated Fermi energies, parallel masses, and band gaps from the 8×8 EFA model.

Superlattice	InAs width (Å)	GaSb width (Å)	Sheet carrier concentration per period ($\times 10^{10}$ cm^{-2})	Fermi energy (meV)	Calculated parallel mass (8×8 EFA)	Measured mobilities (cm^2/V-sec)	Calculated band gaps (meV) InSb-IFs
SL2	41.1	24.0	1.8	13.38	0.0306	747	120.2
SL3	53.6	24.0	2.4	15.19	0.0291	5043	66.6
SL4	62.3	24.0	3.2	17.73	0.0279	8980	47.3
SL5	72.7	24.0	3.0	16.62	0.0261	15450	43.0

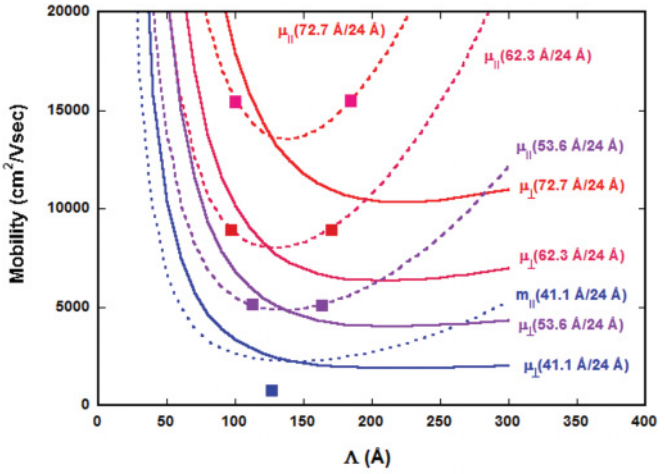

FIG. 12. (Color online) The calculated vertical (continuous) and horizontal (dashed) mobilities for four samples for which low-temperature in-plane mobilities (denoted by squares) are available (see Table II).

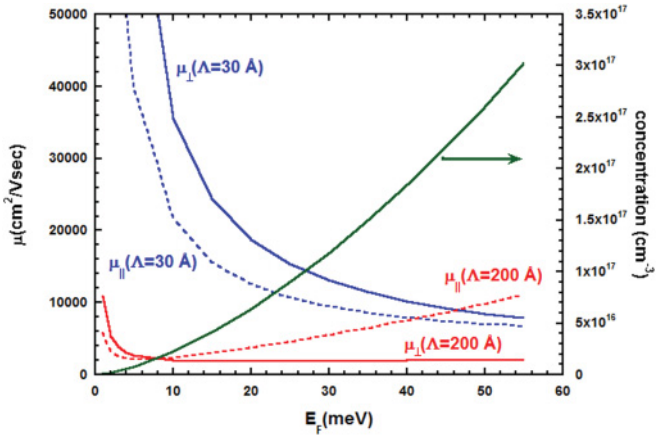

FIG. 13. (Color online) Calculated IRS-limited mobilities for a 41.1Å InAs/24Å GaSb SL with screening for two values of the autocorrelation length as a function of the Fermi level. The carrier concentrations corresponding to the given Fermi level can be read off along the right-hand scale.

respect to vertical rates. Hence, with screening included, it is possible for vertical mobilities to be larger than horizontal mobilities.

As an example of a screened calculation, Fig. 12 shows the calculated mobilites for the parameters of the four samples studied earlier (Table II).[38] Given the experimentally measured carrier concentrations, the Fermi levels for all the samples were calculated from Eq. (24) using the theoretically calculated band dispersions $\varepsilon(k_z)$. For the sheet carrier concentrations per period on the order of 3.0×10^{10} cm^{-2} (Table II), the Fermi energies for the four samples are between 13.38 and 17.73 meV. Vertical roughness Δ is taken to be one monolayer, and the correlation length is left as a free parameter. Figure 12 spans the range of correlation lengths found experimentally by scanning tunneling microscopy by Lew *et al.* [41] ($\Delta = 1.9 \pm 0.1$ Å, $\Lambda = 112 \pm 16$ Å; $\Delta = 2.8 \pm 0.2$ Å, $\Lambda = 174 \pm 21$ Å) for InAs on InGaSb and ($\Delta = 3.2 \pm 0.2$ Å, $\Lambda = 301 \pm 39$ Å; $\Delta = 4.3 \pm 0.2$ Å, $\Lambda = 327 \pm 38$ Å) for InGaSb on InAs interfaces in (110)/(1–10) cross-sections, and by Feenstra *et al.* [42] ($\Delta = 1.8$ Å, $\Lambda = 19$ Å) for InAs on GaSb and ($\Delta = 2.5$ Å, $\Lambda = 40$ Å) for GaSb on InAs interfaces. The calculated mobilities together with the measured data are shown in Fig. 12.

As in the case of quantum wells,[32] the horizontal mobility is a double-valued function of Λ, with a minimum corresponding to the value of Λ comparable to the Fermi wavelength, where the carriers experience the greatest scattering. To the left of the minimum, the electron averages over the small-scale roughness, so the mobility is high. To the right of the minimum, the electron wavelength is smaller than Λ, and the interface appears smooth for in-plane transport, and the mobility is high again. Vertical mobility reaches a steady-state value, since once the interface is sufficiently smooth, scattering becomes specular and depends only on vertical roughness.[23] For low values of Λ, the vertical mobilities are larger than the horizontal mobilities by a factor of approximately 3 to 2. For Λ around 225 Å, the horizontal mobilities are twice as large as the vertical mobilities; for Λ around 300 Å, that ratio is about 3 to 1.

Using the assumed value of Δ, two values of Λ will fit the experimental mobilities for the three widest samples, but no value of Λ will fit the experimental mobility for the narrowest SL. Since mobilities are inversely proportional to the square of vertical roughness, one can achieve agreement with experiment by simply adjusting the value of Δ. However, we also considered possible problems with the measurement and theory. Experimentally, we find that at InAs widths greater than 40 Å samples type-convert from p to n, which may indicate a more complicated physics than assumed in the theory. In addition, there is great sample-to-sample variability in mobilities, depending on the exact growth conditions. Theoretically, there may also be other sources of scattering. For example, we considered the effect of possible alloy scattering due to antimony interdiffusion into InAs[43] but found the strength of such scattering to be two orders of magnitude too small to account for the observed discrepancy between experiment and theory (see Appendix B).

Since the ratio of the two mobilities is independent of Δ, curves like those in Fig. 12 make it possible to estimate the values of vertical mobilities given the measured value of the corresponding horizontal mobility, if an additional piece of information such as horizontal roughness or correlation length are known. Alternatively, horizontal mobility measurements over an extended temperature range may provide enough additional information to make an independent determination of Λ unnecessary.

An example of the concentration dependence of mobilities is given in Fig. 13 for a 41.1Å InAs/24Å GaSb SL for two values of correlation length. For a small correlation length, $\Lambda = 30$ Å, both mobilities decrease as a function of the Fermi level or, equivalently, the carrier density. For the long correlation length of $\Lambda = 200$ Å, the horizontal mobility first decreases and then rises again, while the vertical mobility decreases to an asymptotic value. This behavior is consistent with that in Fig. 12, except that in Fig. 13 the correlation length is fixed and the minimum is found at the Fermi energy corresponding to the Fermi wavelength on the order of the fixed correlation length.

For $\Lambda = 30$Å the minimum takes place at carrier densities beyond the range of the graph.

IV. CONCLUSIONS

The theory of low-temperature electron transport in SLs was presented, treating vertical and horizontal mobilities on an equal footing within the same IRS model. Low temperature vertical and horizontal electron mobilities in InAs/GaSb SLs were calculated by solving the corresponding Boltzmann equations using the energy spectra and wave functions obtained from the solution of the coupled envelope-function Hamiltonians (3×3 for the vertical and 8×8 for the horizontal dispersions) for the SL. The behavior of the scattering rates and mobilities was examined as a function of SL parameters and explained in terms of the underlying physics. In absence of screening a theorem was derived showing that vertical scattering rates are greater than the horizontal rates so that the vertical mobilities should be generally smaller than horizontal mobilities. With screening included, backward scattering in horizontal transport is accentuated, so that no general predictions can be made. The calculated mobilities were found to be strong functions of the interface roughness parameters, carrier concentration, and carrier screening. Theoretically calculated mobilities compared favorably with limited low-temperature, horizontal mobility data on four selected samples. Using the present results and the measured values of horizontal mobilities, it is possible to estimate the value of the corresponding vertical mobilities.

ACKNOWLEDGMENTS

The work of FS was supported by the AF Contract FA8650-11-D-5401 at the Materials and Manufacturing Directorate, AFRL/RXPS. FS would like to thank Y. Fu (KTH, Sweden) for useful discussions regarding alloy scattering.

APPENDIX A

In order to evaluate the quantum-well limit of the expression for mobility, it is necessary to find the product of well height and the fourth power of the modulus of the wave function in the limit of infinite barrier height.[21] Let the quantum well of height V_0 be located between $-a \leqslant z \leqslant a$. The electron-wave function in the ground state is

$$\varphi(z) = \begin{cases} A\cos kz & -a \leqslant z \leqslant a \\ Be^{-\kappa z} & |z| > a \end{cases}, \tag{A1}$$

where $k = \sqrt{2m^*E/\hbar^2}$ and $\kappa = \sqrt{2m^*(V_0 - E)/\hbar^2}$. The boundary conditions on the wave function and its derivative furnish the relation $\varphi(a)/\varphi'(a) = -1/\kappa$, so that

$$V_0^2\varphi^4(a) = V_0^2\left(\varphi'(a)/\kappa\right)^4 = V_0^2\left(\frac{\hbar^2}{2m^*(V_0 - E)}\right)^2 \times (kA\sin ka)^4. \tag{A2}$$

In the limit of infinite barrier height, the amplitude $A = 1/\sqrt{a}$, $k = \pi/2a$, and $\sin ka = 1$, so that

$$\lim_{V_0\to\infty} V_0^2\varphi^4(a) = (\hbar^2\pi^2/m^*)^2/(2a)^6. \tag{A3}$$

Inserting this dependence into the expression for the relaxation rate gives

$$\frac{1}{\tau_{||}(\mathbf{k})} = \left(\frac{\ell}{4\pi\hbar}\frac{\pi^4\hbar^4\Delta^2\Lambda^2}{(m^*)^2(2a)^6}\right)\int_{-\pi/l}^{\pi/l} dk_z' \times \int (1-\cos\theta')\exp(-\Lambda^2(\mathbf{k}_{||}' - \mathbf{k}_{||})^2/4) \times \delta(\varepsilon - \varepsilon')d^2\mathbf{k}_{||}', \tag{A4}$$

and using $\varepsilon(\mathbf{k}_{||}) = \hbar^2k_{||}^2/2m^*$, the k_z integral gives $2\pi/\ell$. Integrating over $\mathbf{k}_{||}'$ with $\delta(\varepsilon - \varepsilon') = m^*\delta(k_{||}' - k_{||})/(\hbar^2k_{||})$, the final result is

$$\frac{1}{\tau_{||}(k_{||})} = \left(\frac{\pi^4\hbar\Delta^2\Lambda^2}{2m^*(2a)^6}\right)\int (1-\cos\theta') \times \exp\left(-\Lambda_i^2k_{||}^2\frac{1-\cos\theta'}{2}\right)d\theta', \tag{A5}$$

so that $\tau_{||}$ and mobility are proportional to the sixth power of layer width. This agrees with the expression for quantum wells derived by Gold.[32] The relaxation rate in the vertical direction has the same functional dependence but without the $\cos\theta'$ term. Hence, the present theory correctly reduces to the quantum-well limit as the barrier height becomes infinite.

APPENDIX B: ESTIMATE OF ALLOY SCATTERING

In this section we develop an expression for the relaxation time in SLs for alloy scattering in order to compare the strengths of alloy and IRS scatterings. In the binary-binary SL, alloy scattering can be due to Sb interdiffusion into InAs layers, which results in an $InAs_{1-x}Sb_x$ alloy with the alloy profile $x(z)$. In order to calculate the relaxation rates for alloy scattering,[44] the potential in the current-carrying region is written in the virtual crystal form as[45]

$$V_0(\mathbf{r}) = \sum_{\mathbf{a}}[xV_{\mathrm{InSb}}(\mathbf{r}-\mathbf{a}) + (1-x)V_{\mathrm{InAs}}(\mathbf{r}-\mathbf{a})], \tag{B1}$$

where the sum is over all the molecular sites. Scattering is due to random deviations from the average crystal,

$$\delta V_0(\mathbf{r}) = \sum_{\mathbf{a}} c_{\mathbf{a}}[V_{\mathrm{InSb}}(\mathbf{r}-\mathbf{a}) - V_{\mathrm{InAs}}(\mathbf{r}-\mathbf{a})], \tag{B2}$$

where $c_{\mathbf{a}}$ is a random function equal to

$$c_{\mathbf{a}} = \begin{cases} 1-x & \text{for an InSb molecule at } \mathbf{a}, \\ -x & \text{for an InAs molecule at } \mathbf{a}, \end{cases} \tag{B3}$$

and the scattering potential is

$$V_{\mathrm{InSb}}(\mathbf{r}-\mathbf{a}) - V_{\mathrm{InAs}}(\mathbf{r}-\mathbf{a}) \equiv \nu_0\omega_0\delta(\mathbf{r}-\mathbf{a}), \tag{B4}$$

where $\omega_0 = a^3/4$ is the volume per anion-cation pair[46] and ν_0 is the conduction-band offset between InSb and InAs.

The matrix element of the scattering potential is calculated to be

$$|M(\mathbf{k},\mathbf{k}')|^2 = \delta_{\mathbf{k}_{||},\mathbf{k}'_{||}} \left(\frac{\nu_0^2\omega_0}{A}\right) \int [1-x(z)]x(z)|\phi_{k_z}(z)|^2 \times |\phi_{k'_z}(z)|^2 dz, \quad \text{(B5)}$$

which, like IRS, is also randomizing and elastic. Since the scattering mechanism is isotropic and independent of the scattering angle θ', the in-scattering term for the horizontal relaxation rate integrates to zero, so that the horizontal and vertical relaxation times are equal,

$$\frac{1}{\tau_\perp(E,k_z)} = \frac{1}{\tau_{||}(E,k_z)} = \frac{\ell m_{||}}{2\pi\hbar^3}\left(\nu_0^2\omega_0\right) \times \int \mathrm{I}(k_z,k'_z)\Theta(E-\varepsilon'_z)dk'_z, \quad \text{(B6)}$$

where

$$\mathrm{I}\left(k_z,k'_z\right) \equiv \int_0^l (1-x(z))x(z)|\phi_{k_z}(z)|^2|\phi_{k'_z}(z)|^2 dz \quad \text{(B7)}$$

is the overlap of the grading profile with the initial and final state wave functions. Equation (B6) agrees with the similar expressions derived earlier for quantum wells.[47–49]

To compare alloy to IRS scattering, we assume that Sb diffuses into InAs at both interfaces by about one monolayer, $\delta \approx 3A$, so that

$$x(z) = \begin{cases} 1-(z+a)/\delta & -a \leqslant z \leqslant -a+\delta \\ 0 & -a+\delta \leqslant z \leqslant a-\delta \\ 1+(z-a)/\delta & a-\delta \leqslant z \leqslant a \end{cases}. \quad \text{(B8)}$$

Inserting this profile into Eq. (B6), one may approximate the relaxation rate by

$$\frac{1}{\tau_\perp(E,k_z)} = \left(\frac{m_{||}\ell}{\hbar^3}\nu_0^2|\phi_{k_z}(a)|^2\right)\frac{\delta\omega_0}{3\pi} \times \int_0^{\pi/\ell} |\phi_{k'_z}(a)|^2\Theta(E-\varepsilon'_z)dk'_z. \quad \text{(B9)}$$

The difference between Eq. (B4) for alloy scattering and Eqs. (39) and (40) for IRS scattering is mainly in the strength parameters: $\nu_0^2\delta\omega_0/3\pi$ for alloy scattering and $2V_0^2\Omega^2\Lambda^2$ for IRS. Inserting typical numbers for the InAs/GaSb SL shows that alloy scattering is about 100 times weaker than IRS scattering.

*frank.szmulowicz.ctr@wpafb.af.mil

[1] A. Rogalski and P. Martyniuk, Infrared Phys. Technol. **48**, 39 (2006); A. Rogalski, J. Antoszewski, and L. Faraone, J. Appl. Phys. **105**, 091101 (2009).

[2] Q. K. Yang, F. Fuchs, J. Schmitz, and W. Pletschen, Appl. Phys. Lett. **81**, 4757 (2002).

[3] R. Rehm, M. Walther, F. Fuchs, J. Schmitz, and J. H. Fleissner, Appl. Phys. Lett. **86**, 173501 (2005).

[4] B.-M. Nguyen, D. Hoffman, E. K.-W. Huang, P.-Y. Delaunay, and M. Razeghi, Appl. Phys. Lett. **93**, 123502 (2008); S. A. Pour, E. K. Huang, G. Chen, A. Haddani, B.-M. Nguyen, and M. Razeghi, *ibid.* **98**, 143501 (2011).

[5] A. Hood, M. Razeghi, E. H. Aifer, and G. J. Brown, Appl. Phys. Lett. **87**, 151113 (2005).

[6] H. J. Haugan, F. Szmulowicz, K. Mahalingam, G. J. Brown, S. R. Munshi, and B. Ullrich, Appl. Phys. Lett. **87**, 261106 (2005).

[7] F. Szmulowicz, H. J. Haugan, G. J. Brown, K. Mahalingam, B. Ullrich, S. R. Munshi, and L. Grazulis, Opto-Electronics Rev. **14**, 69 (2006).

[8] E. Plis, J. B. Rodriguez, G. Balakrishnan, Y. D. Sharma, H. S. Kim, T. Rotter, and S. Krishna, Semicond. Sci. Technol. **25**, 085010 (2010).

[9] W. W. Bewley, J. R. Lindle, C. S. Kim, M. Kim, C. L. Canedy, I. Vurgaftman, and J. R. Meyer, Appl. Phys. Lett. **93**, 041118 (2008).

[10] J. B. Rodriguez, C. Cervera, and P. Christol, Appl. Phys. Lett. **97**, 251113 (2010).

[11] F. Aristone, J.-C. Portal, J. F. Palmier, and J. C. Harmand, Braz. J. Phys. **29**, 375 (1999); A. Sibille, J. F. Palmier, H. Wang, and F. Mollot, Phys. Rev. Lett. **64**, 52 (1990); F. Aristone, P. Gassot, J. F. Palmier, D. K. Maude, B. Goutiers, J. L. Gauffier, J. C. Portal, and G. Mollot, Superlattices Microstruct. **15**, 225 (1994).

[12] G. A. Umana-Membreno, H. Kala, J. Antoszewski, J. M. Dell, L. Faraone, B. Klein, G. Gautam, M. N. Kutty, E. Plis, and S. Krishna, Proc. SPIE **8012**, 80120Y (2011).

[13] L. Bürkle, F. Fuchs, R. Kiefer, W. Pletschen, R. E. Sah, and J. Schmits, Mater. Res. Soc. Symp. Proc. **607**, 77 (2000).

[14] F. Fuchs, E. Ahlswede, U. Weimar, W. Pletschen, J. Schmitz, M. Hartung, B. Jager, J. P. Kotthaus, and F. Szmulowicz, Appl. Phys. Lett. **73**, 3760 (1998).

[15] C. A. Hoffman, J. R. Meyer, E. R. Youngdale, F. J. Bartoli, and H. R. Miles, Appl. Phys. Lett. **63**, 2210 (1993); J. R. Meyer, D. J. Arnold, C. A. Hoffman, and F. J. Bartoli, *ibid.* **58**, 2523 (1991).

[16] J. F. Palmier and A. Chomette, J. Physique **43**, 381 (1982); L. Friedman, Phys. Rev. B **32**, 955 (1985).

[17] T. Ando, J. Phys. Soc. Jpn. **51**(12), 3900 (1982).

[18] R. W. Prange and T. W. Nee, Phys. Rev. **168**, 779 (1986); H. Sakaki, T. Noda, K. Hirakawa, M. Tanaka, and T. Matsusue, Appl. Phys. Lett. **41**, 1934 (1987); T. Noda, M. Tanaka, and H. Sakaki, *ibid.* **57**, 1651 (1990); U. Penner, H. Rücker, and I. N. Yassievich, Semicond. Sci. Technol. **13**, 709 (1998); N. Balkan, R. Gupta, M. Cankurtaran, H. Çelik, A. Bayrakli, E. Tiras, and M. Ç. Arikan, Superlattice Microstr. **22**, 263 (1997); R. Nag, S. Mukyopadhyay, and M. Das, J. Appl. Phys. **86**, 459 (1999); J. M. Li, J. J. Wu, X. X. Han, Y. W. Lu, X. L. Liu, Q. S. Zhu, and Z. G. Wang, Semicond. Sci. Technol. **20**, 1207 (2005); B. R. Nag, *ibid.* **19**, 162 (2004); A. Gold, J. Appl. Phys. **103**, 043718 (2008).

[19] F. Szmulowicz and G. J. Brown, Appl. Phys. Lett. **98**, 182105 (2011); Proc. SPIE **7945**, 79451U (2011).

[20] S. Mori and T. Ando, J. Phys. Soc. Jpn. **48**(3), 865 (1980).

[21] I. Dharssi and P. N. Butcher, J. Phys. Condens. Matter **2**, 119 (1990).

[22]F. Aristone, P. Gassot, J. F. Palmier, D. K. Maude, B. Goutiers, J. L. Gauffier, J. C. Portal, and F. Mollot, Superlattices Microstruct. **5**, 225 (1994); J. Q. You, L. Zhang, and Q. B. Yang, Phys. Rev. B **55**, 15757 (1997); G. J. Warren and P. N. Butcher, Semicond. Sci. Technol. **1**, 133 (1986).

[23]G. Etemadi and J. F. Palmier, Solid State Commun. **86**, 739 (1993).

[24]J. R. Meyer, D. J. Arnold, C. A. Hoffman, F. J. Bartoli, and L. R. Ram-Mohan, Phys. Rev. B **46**, 4139 (1992); C. A. Hoffman, J. R. Meyer, E. R. Youngdale, F. J. Bartoli, R. H. Miles, and L. R. Ram-Mohan, Solid-State Electron. **37**, 1203 (1994); Y. A. Pusep, G. C. Gozzo, and R. R. LaPierre, Appl. Phys. Lett. **93**, 24214 (2008); T. V. Chandrasekhar Rao, J. Antoszewski, L. Faraone, J. B. Rodriguez, E. Plis, and S. Krishna, *ibid*. **92**, 012121 (2008); C. Cervera, J. B. Rodrigue, J. P. Perez, H. Ait-Kaci, R. Chaghi, L. Konczewicz, S. Contreras, and P. Christol, J. Appl. Phys. **106**, 033709 (2009).

[25]G. Bastard, *Wave Mechanics Applied to Semiconductor Heterostructures,* (Halsted, New York, 1988), p. 43.

[26]F. Szmulowicz, H. Haugan, and G. J. Brown, Phys. Rev. B **69**, 155321 (2004).

[27]F. Szmulowicz, E. R. Heller, and K. Fisher, Superlattices Microstructures **17**, 373 (1995).

[28]Chris G. Van de Walle, Phys. Rev. B **39**, 1871 (1989).

[29]*Numerical Data and Functional Relationships in Science and Technology*, edited by O. Madelung, Vol. 17a, b, Group 3 of Landolt-Borstein (Springer, New York, 1982).

[30]K. C. Hass and D. J. Kirill, Phys. Rev. B **44**, 7042 (1990).

[31]J. R. Meyer, D. J. Arnold, C. A. Hoffman, and F. J. Bartoli, App. Phys. Lett. **58**, 2523 (1991).

[32]A. Gold, Phys. Rev. B **35**, 723 (1987).

[33]M. Wataya, N. Sawaki, H. Goro, I. Akasaki, H. Kano, and M. Hashimoto, Jpn. J. Appl. Phys. **28**, 1934 (1989).

[34]B. R. Nag, *Theory of Electrical Transport in Semiconductors,* (Pergamon, New York (1972), pp. 75–118.

[35]B. R. Nag, *Electron Transport in Compound Semiconductors,* (Springer, New York, 1980), pp. 93–128.

[36]See, e.g., J. R. Meyer, D. J. Arnold, C. A. Hoffman, and F. J. Bartoli, J. Appl. Phys. **74**, 6676 (1993); J. M. Ziman, *Principles of the Theory of Solids*, 2nd ed. (Cambridge, University Press, London, 1972), Chap. 7.

[37]M. Abramowitz and Irene A. Stegun, *Handbook of Mathematical Functions: with Formulas, Graphs, and Mathematical Tables,* (Dover, New York, 1964), p. 374.

[38]F. Szmulowicz, S. Elhamri, H. J. Haugan, G. J. Brown, and W. C. Mitchel, J. Appl. Phys. **101**, 043706 (2007); **105**, 074393 (2009).

[39]Owing to a numerical problem, Ref. 19 incorrectly showed a structure in the mobility vs InAs thickness curve at 60 Å, the transition point between the decaying and oscillatory wave behavior in GaSb.

[40]T. Ando, A. B. Fowler, and F. Stern, Rev. Mod. Phys. **54**, 437 (1982); J. R. Meyer, D. J. Arnold, C. A. Hoffman, and F. J. Bartoli, J. Appl. Phys. **74**, 6676 (1993).

[41]A. Y. Lew, S. L. Zuo, E. T. Yu, and R. H. Miles, Appl. Phys. Lett. **70**, 75 (1997); Phys. Rev. B **57**, 6534 (1998).

[42]R. M. Feenstra, D. A. Collins, D. Z.-Y. Ting, M. W. Wang, and T. C. McGill, Phys. Rev. Lett. **72**, 2749 (1994).

[43]J. Steinshnider, J. Harper, M. Weimer, C.-H. Lin, S. S. Pei, and D. H. Chow, Phys. Rev. Lett. **85**, 4562 (2000).

[44]L. Nordheim, Ann. Phys. **401**, 607 (1931).

[45]Y. Fu and M. Willander, J. Appl. Phys. **88**, 288 (2000).

[46]D. N. Quang, N. H. Tung, D. T. Hien, and H. A. Huy, Phys. Rev. B **75**, 073305 (2007).

[47]G. Bastard, Surf. Sci. **142**, 284 (1984).

[48]J. M. Li, J. J. Wu, X. X. Han, Y.W. Lu, X. L. Liu, Q. S. Zhu, and Z. G. Wang, Semicond. Sci. Technol. **20**, 1207 (2005).